JGR Space Physics

RESEARCH ARTICLE
10.1029/2023JA031779

Efficient Resonant Fast-Alfvén Wave Coupling as a Minimization Principle

Andrew N. Wright[1]

[1]School of Mathematics and Statistics, University of St Andrews, St Andrews, UK

Key Points:

- The Resonance Map formulation of resonant fast and Alfvén wave coupling is consolidated
- It is shown that the locations where the strongest coupling occurs can be identified using a minimization principle

Correspondence to:

A. N. Wright,
anw@st-and.ac.uk

Citation:

Wright, A. N. (2023). Efficient resonant fast-Alfvén wave coupling as a minimization principle. *Journal of Geophysical Research: Space Physics*, *128*, e2023JA031779. https://doi.org/10.1029/2023JA031779

Received 13 JUN 2023
Accepted 15 NOV 2023

Abstract The resonant coupling of the fast magnetosonic wave to the Alfvén wave is considered in the ideal magnetohydrodynamic limit in a 3D equilibrium. It has previously been shown that the most efficient coupling occurs on particular paths that satisfy the "tangential alignment condition" (Wright et al., 2022, https://doi.org/10.1029/2022ja030294). In this article we show how this criterion is equivalent to a minimization principle which may lead to a deeper understanding of the physics of the wave coupling process.

1. Introduction

The resonant excitation of standing Alfvén waves by the magnetosonic fast mode is a key processes in magnetospheric physics that has been used to interpret magnetic pulsations for half a century (Chen & Hasegawa, 1974; Samson et al., 1971; Southwood, 1974). The same resonant coupling process occurs in the solar corona in magnetic loops and arcades. (See the reviews by Goossens et al. (2011) and Van Doorsselaere et al. (2020) and references therein.) Theory for both solar and magnetospheric applications was reduced to 1D (Allan et al., 1986; Goossens et al., 1995; Mann et al., 1995; Poedts et al., 1989). Later this was extended to describe wave coupling in 2D equilibria (Thompson & Wright, 1993; Tirry & Goossens, 1995; Wright & Thompson, 1994). Related theory has also been developed in a laboratory plasma context for 2D equilibria (Goedbloed, 1975; Pao, 1975). More recently, the theory of this process has been developed in realistic 3D equilibria (Cheng, 2003; Degeling et al., 2010, 2018; Terradas et al., 2016; Wright & Elsden, 2016). A review of this area has been published by Elsden et al. (2022).

The above studies have adopted a number of approaches. Some have considered normal modes ($\propto \exp(i\omega t)$) of the governing (linear) equations. Each such mode remains decoupled from other normal modes and, by itself, does not represent a causal solution. However, a suitable sum of these modes can be used to construct a time-dependent physical solution which does obey causality. Moreover, this is even true for ideal normal modes that may contain resonant singularities. If dissipation is included (or complex ω considered) the normal modes become non-singular and have a more direct relation to time dependent solutions, as they can represent the large time limit of a suitable steadily driven time-dependent simulation. Such modes may contain perturbations that have the character of fast waves near a driven boundary, and the character of Alfvén wave on the resonant field lines. Hence, it is possible to interpret this solution physically in terms of the coupling of a fast wave to an Alfvén wave, even though it is a single normal mode of the governing equations.

The theory of wave coupling in 3D contains features that are not present in 1D and 2D modeling. In particular, there are several locations and polarizations that the resonant Alfvén waves could adopt. In a particular situation, it appears that one or two of the possibilities are favored. Wright and Elsden (2016) show how boundary conditions can determine the solution. However, if the resonant Alfvén waves do not encounter the simulation boundaries an alternative criterion has been proposed—termed the "tangential alignment condition" (Wright et al., 2022).

In this article we consolidate the formulation leading to the tangential alignment condition and show that it is equivalent to a minimization problem. Minimization problems have a rich history in mathematical physics. For example, in 1662 Fermat proposed the principle of least time: when light travels between two points in space, it follows a path that minimizes the travel time. In 1744 Maupertuis proposed the principle of least action (also known as Hamilton's principle): the path taken by a physical system between two points in space and time is the one that minimizes the action (i.e., the time integral of the Lagrangian). In 1774 Lagrange suggested the principle of least area: soap films adopt a configuration that minimizes their area. More recently, the principle of least resistance was realized: in an electrical circuit current flows to minimize ohmic heating.

The existence of minimization principles has proven to be extremely valuable as they often point to some deeper truth about the nature of the system in question. For example, Fermat's principle of least time points to light having a wave-like nature. The principle of least action points to matter, at a deeper level, being quantum mechanical (Feynman, 1964). The principle of least area points to a soap film not really being a liquid, but a collection of molecules adopting the lowest energy configuration. Hence it is intriguing to see a minimization principle operating in a resonant wave coupling problem.

The paper is structured as follows: Section 2 establishes a formalism for discussing Alfvén wave frequency and polarization, along with the related concepts of the Resonant Zone and Resonant Paths; Section 3 considers the analytical form of Resonant Paths and provides an approximation for them along with examples; Section 4 shows how the tangential alignment condition can be recast as a minimization principle and gives a worked example to verify this assertion; Section 5 gives some concluding remarks.

2. Alfvén Frequency and Polarization

Dungey (1954) considered standing Alfvén waves in an axisymmetric equilibrium poloidal field. Two wave equations were derived: one for axisymmetric Alfvén waves with a plasma displacement in the toroidal direction, and another for highly asymmetric Alfvén waves with a poloidal plasma displacement. It was noted that the frequencies of these two waves (the toroidal and poloidal Alfvén frequencies) are different. For example, in a 3D dipole field the toroidal can exceed the poloidal frequency by over 30%, while in a 2D (line dipole) field the difference can be as much as 300% (Elsden, 2016). Note that we use the term "3D dipole" to refer to the far field axisymmetric poloidal field lines formed by a ring of current flowing in the azimuthal direction around the origin. A "2D dipole" refers to the field produced by a pair of equal and opposite closely spaced line currents (so is also referred to as a "line dipole"). If the line currents are aligned with, say, the Cartesian $\mathbf{e}_y$ direction, the equilibrium will be independent y, and the field lines confined to planes of $y = const$. Although the 2D and 3D dipoles are independent of a coordinate (y and azimuth, respectively), they can still be used to study wave coupling in three-dimensional equilibria by allowing the plasma density (and Alfvén speed) to vary in three dimensions.

The toroidal and poloidal wave equations can be cast in terms of field-aligned coordinates (Singer et al., 1981). Typically coordinates (α, β, γ) are used, where α and β are two transverse coordinates that are constant on a given field line, and so their values can be used as labels to identify a particular field line. The coordinate γ is used to parameterize position along the field line. Thus, we can think of the Alfvén frequency as being a property of the field line and the wave's polarization angle. Alternatively, we can imagine the intersection of the field lines with a reference plane, such as the equatorial plane, and use the values (x, y) where the field line intersects that plane to identify the field line. The Alfvén wave polarization angle can be defined as the angle between the Alfvén wave plasma displacement (ξ_x, ξ_y) and a reference direction, for example, the toroidal direction (Wright & Elsden, 2016). In this convention $\theta = 0$ corresponds to the toroidal polarization, and $\theta = \pi/2$ to the poloidal.

Wright and Elsden (2016) generalized the field aligned coordinate formulation to include Alfvén waves whose polarization lies between the limits of toroidal and poloidal. In general we have $\omega_A(x, y, \theta)$, that is, the Alfvén frequency (ω_A) depends upon which field line we are considering (x and y) and the wave's polarization (θ). Figure 1a shows the typical variation of ω_A with θ for a 2D or 3D dipole field for a given field line. The curve is periodic with period of π. The axisymmetry of the equilibrium poloidal field means $\omega_A(\theta) = \omega_A(-\theta)$, so the maximum and minimum ω_A will occur for either $\theta = 0$ (toroidal) or $\theta = \pi/2$ (poloidal). For dipole fields the toroidal frequency exceeds the poloidal frequency, and the red dots in Figure 1a indicate the values of θ where ω_A has its maximum and minimum values, namely at θ_{max} and θ_{min}.

For the case of a non-axisymmetric field the $\omega_A(\theta)$ curve has a generic form like that in Figure 1b. Wright et al. (2022) considered the case of a compressed dipole, and they found that the vast majority of field lines retained one maximum and one minimum. Formally, we can identify the values of θ_{max} and θ_{min} as the roots of the equation

$$\left.\frac{\partial \omega_A(x, y, \theta)}{\partial \theta}\right|_{x,y} = 0 \Rightarrow \theta_{\max}(x, y) \text{ and } \theta_{\min}(x, y), \tag{1}$$

and so can identify the maximum and minimum Alfvén frequencies for all field lines, expressed as functions of the labels x and y

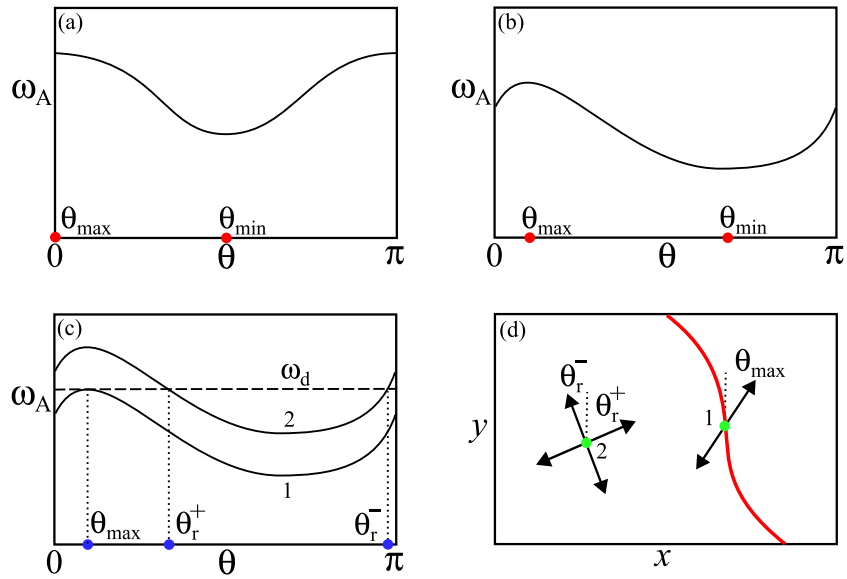

Figure 1. (a) The variation of ω_A with polarization angle, θ. The polarization angle is measured relative to a reference direction, such as the toroidal direction. The variation shown is typical of a potential field that has an invariant coordinate, such as 2D line dipole or a 3D axisymmetric dipole. In these cases the minimum and maximum ω_A occur for polarization angles θ_{min} and θ_{max} corresponding to the poloidal and toroidal directions. (b) Typical variation of $\omega_A(\theta)$ for a field without an invariant coordinate. (c) The variation of $\omega_A(\theta)$ for two field lines along with the driving frequency, ω_d (dashed line). The blue dots indicate the resonant polarization angles. (d) Part of the Resonance Map in the (x, y) plane. The green dots indicate the intersection of field lines 1 and 2 (from panel (c)) with the plane. Polarization angles are measured relative to the y direction, and the black arrows indicate the direction of the resonant Alfvén wave displacement (ξ_x, ξ_y). The red line denotes the Resonant Zone boundary.

$$\omega_{A\max}(x, y) = \omega_A(x, y, \theta_{\max}(x, y)), \qquad \omega_{A\min}(x, y) = \omega_A(x, y, \theta_{\min}(x, y)). \tag{2}$$

In terms of functional relations we can express the dependence of ω_A on x, y, and θ through a function f_0, which can, in principle, be inverted to give θ in terms of x, y, and ω_A through a new function f_1,

$$\omega_A = f_0(x, y, \theta) \qquad \Rightarrow \qquad \theta = f_1(x, y, \omega_A). \tag{3}$$

For a given field line (x and y), and chosen ω_A, the latter relation tells us the required polarization, θ, for that particular field line to have our chosen frequency. From the curves in Figures 1a and 1b it is evident that there will be no solutions for θ if we choose ω_A to be greater than $\omega_{A\max}(x, y)$ or less than $\omega_{A\min}(x, y)$. If $\omega_{A\min}(x, y) < \omega_A < \omega_{A\max}(x, y)$ there will be two distinct single root solutions for θ, while if $\omega_A = \omega_{A\min}(x, y)$ or $\omega_A = \omega_{A\max}(x, y)$ there will be one double root solution at $\theta_{min}(x, y)$ or $\theta_{max}(x, y)$.

2.1. Resonant Polarization and Boundaries

In the case of resonantly driven Alfvén waves, the fast mode acts as a driver. We denote the driving frequency of this mode by ω_d. This is represented by the horizontal dashed line in Figure 1c. We can now ask whether it is possible for a particular field line to support a resonant Alfvén wave at the driving frequency, ω_d, and, if so, what polarization will it have? For the field line corresponding to the curve labeled 2, we see that the resonant condition $\omega_A = \omega_d$ has two single roots at angles θ_r^+ and θ_r^- (see the blue dots in Figure 1c). On a different field line (corresponding to curve labeled 1) there is only one resonant polarization given by $\theta_r = \theta_{max}$. (We use the notation of the subscript "r" to denote that the polarization angle satisfies the resonant condition.)

Figure 1d shows the locations (in the (x, y) plane) of the two field lines labeled 1 and 2 and shown as green dots. The black arrows are inclined to the y direction (the dotted line) by θ_r. Field line 1 is special in that the resonant condition is satisfied for the maximum ω_A on that field line, so there is only one value of θ_r. The same will be true of a different field line where the minimum ω_A matches ω_d. The locations of these field lines can be considered further by defining the functions

$$\Gamma_{\max}(x, y, \omega_d) = \omega_{A\max}(x, y) - \omega_d, \qquad \Gamma_{\min}(x, y, \omega_d) = \omega_{A\min}(x, y) - \omega_d. \tag{4}$$

Evidently, the double roots of the resonant condition (where there is a unique θ_r) are found in the (x, y) plane by setting $\Gamma_{\max}(x, y, \omega_d)$ and $\Gamma_{\min}(x, y, \omega_d)$ to zero. This will give an implicit equation for a curve in the (x, y) plane, and we denote the corresponding values as $(x_{\max}, y_{\max})$ and $(x_{\min}, y_{\min})$.

$$\Gamma_{\max}(x_{\max}, y_{\max}, \omega_d) = 0 \quad \Rightarrow \quad y_{\max}(x_{\max}) \quad \text{or} \quad x_{\max}(y_{\max}), \tag{5}$$

$$\Gamma_{\min}(x_{\min}, y_{\min}, \omega_d) = 0 \quad \Rightarrow \quad y_{\min}(x_{\min}) \quad \text{or} \quad x_{\min}(y_{\min}). \tag{6}$$

The red line in Figure 1d represents the set of points $(x_{\max}, y_{\max})$. Field lines to the left of this line (locally) can satisfy the resonant condition with two solutions for θ_r (that we call θ_r^+ and θ_r^-), so this region is termed the Resonant Zone. Field lines to the right of the red line cannot match the resonant condition, so this region is known as the Non-Resonant Zone, and the red line itself is called the Resonant Zone Boundary. Depending on the details of the equilibrium there can be a further boundaries elsewhere, and some of these could correspond to where $\Gamma_{\min} = 0$. (See Wright and Elsden (2016) and Wright et al. (2022) for some examples.)

2.2. Resonant Paths and the Resonant Zone

When an Alfvén resonance exists, it does not occur on an isolated field line, but on a set of field lines that form a surface in 3D space (see Figure 3c of Wright and Elsden (2016), and Figure 4a of Wright and Elsden (2023)). We now consider the intersection of this surface with the (x, y) plane. Suppose that the field line labeled 2 in Figure 1d supports a resonant Alfvén wave with $\theta_r = \theta_r^-$. Wright and Elsden (2016) show that the plasma displacement (ξ_x, ξ_y) is aligned with this direction and stepping a small distance parallel to this gets us to a new field line with a slightly different value of θ_r. Continuing this process by stepping in the new direction repeatedly allows us to generate the curve in the (x, y) plane corresponding to the intersection with the resonant surface of field lines. We shall refer to this curve as a Resonant Path.

Describing this process mathematically, we begin by identifying the resonant polarization, θ_r, by setting $\omega_A = \omega_d$ in Equation 3,

$$\theta_r = f_1(x, y, \omega_A = \omega_d). \tag{7}$$

In the remainder of this section ω_d plays the role of a parameter, rather than a variable. The ODE for the resonant path is

$$\frac{dx}{dy} = \tan(\theta_r(x, y, \omega_A = \omega_d)) = f_2(x, y, \omega_d) \tag{8}$$

This can be integrated to give $F(x, y, \omega_d) = const$. The constancy of F along a Resonant Path can be interpreted in terms of characteristics: Suppose we parameterize the path by s, so that a particular path is specified by $x(s)$ and $y(s)$. The rate of change of F with s along the path is

$$\frac{dF}{ds} = \left.\frac{\partial F}{\partial x}\right|_y \frac{dx}{ds} + \left.\frac{\partial F}{\partial y}\right|_x \frac{dy}{ds}. \tag{9}$$

If F is constant ($dF/ds = 0$) Equations 8 and 9 give

$$\frac{dx}{dy} = -\frac{\partial F/\partial y|_x}{\partial F/\partial x|_y} \equiv \left.\frac{\partial x}{\partial y}\right|_F = f_2(x, y, \omega_d). \tag{10}$$

The equivalence of the second and third terms above follows from an identity and confirms that the function f_2 in Equation 8 corresponds to how x changes with y when F is constant. As F is constant on a Resonant Path, its value can be used to label these paths.

Solving Equation 8 to get F is rarely analytical and is normally done numerically (Wright & Elsden, 2016; Wright et al., 2022). However, Equation 10 opens up the possibility of facilitating further analytical progress: we can start by making an explicit choice for $F(x, y, \omega_d)$, from which the permissible Resonant Paths immediately follow from the contours of F in the (x, y) plane. The second and fourth terms in Equation 10 then allow the calculation of f_2 for our choice of F. Moreover, we are guaranteed that this f_2 will allow Equation 8 to be integrable analytically.

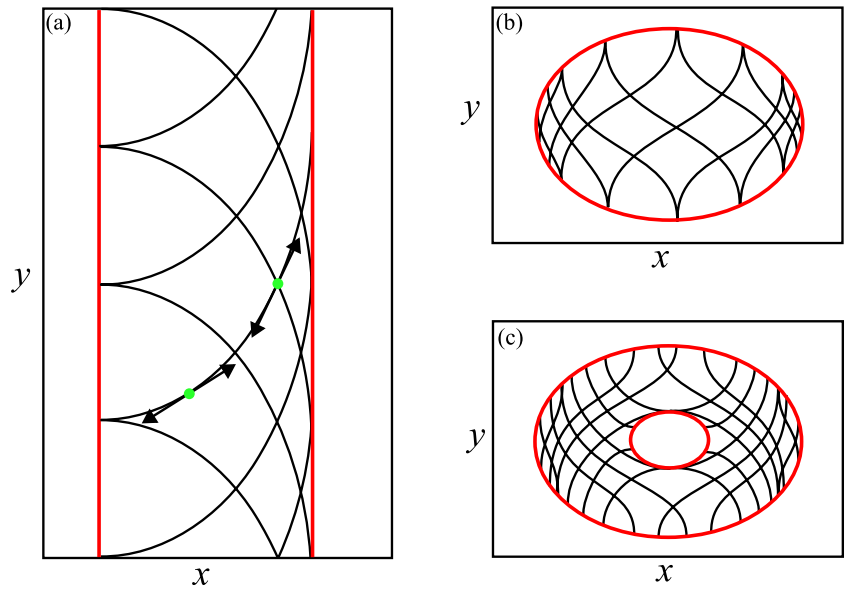

Figure 2. Resonance Maps in the (x, y) plane for an equilibrium field that is independent of y: (a) an example where the density is also independent of y. The left (right) red lines correspond to the $\omega_{Amin} = \omega_d$ ($\omega_{Amax} = \omega_d$) boundaries. The green dots indicate the intersection of resonant field lines with the (x, y) plane. The direction of the plasma displacement is indicated by the black arrows and is tangential to the black lines; (b) the density varies in 3D, but there is only one Resonant Zone boundary; (c) an example where the density varies in 3D and there are two boundaries.

Figure 2 shows some examples of Resonance Maps depicting the Resonant Zone boundaries in red and the Resonant Paths in black. These examples all use an equilibrium field that is invariant in y, so the toroidal direction here corresponds to y, and equilibrium field lines are confined to planes $y = const$. The maximum ω_A on any field line occurs for a toroidal polarization, that is, $\theta_r = 0$ and the plasma displacement is aligned with the unit vector $\mathbf{e}_y$. The minimum ω_A on any field line has a poloidal polarization, that is, $\theta_r = \pi/2$ and the plasma displacement is aligned with the unit vector $\mathbf{e}_x$. The 2D (line) dipole used by Wright and Elsden (2016) is an example of such an equilibrium field.

The variation of ω_A with θ for any field line is qualitatively similar to that in Figure 1a, although the actual values of the frequencies can change from one field line to another. For example, consider two field lines that have the same boundary conditions and magnetic field variation, but the density on one is exactly four times that of the other. The two $\omega_A(\theta)$ curves would have similar form, except the values of the frequencies on one field line would be exactly double those of the other.

In Figure 2a the density is also independent of y but varies with x and z such that $\partial\omega_A/\partial x$ is negative (i.e., the Alfvén frequency decreases with x) in the (x, y) plane. The green dots represent the intersection of two field lines with the (x, y) plane, and the black arrows show the corresponding Alfvén wave plasma displacement. The left hand boundary corresponds to $\Gamma_{min} = 0$ and the paths emerge from it aligned with $\mathbf{e}_x$. As we move along the path the resonant polarization angle changes and reaches the toroidal orientation (aligned with $\mathbf{e}_y$) when it reaches the $\Gamma_{max} = 0$ boundary on the right.

Figure 2b uses the same magnetic field as in (a), but has a more complicated density distribution. There is only one boundary curve, and it is evidently the $\Gamma_{max} = 0$ curve as the paths align with $\mathbf{e}_y$ when they reach the boundary. (Recall that on this boundary $\omega_{Amax}(x, y) = \omega_d$ and for this field $\omega_{Amax}(x, y) = \omega_A(x, y, \theta = 0)$.) As the paths move away from the boundary they start to rotate toward the poloidal direction, but only partially get there. Indeed, at the center of the Resonant Zone the most inclined paths have $\theta_r \approx \pm\pi/4$. In Figure 2c the density change is more extreme than in (b) and the paths now rotate fully to the polarization corresponding to the $\Gamma_{min} = 0$ boundary, which is depicted as the inner loop. On this boundary the paths align with $\mathbf{e}_x$, which is to be expected as $\omega_{Amin}(x, y) = \omega_A(x, y, \theta = \pi/2)$.

3. Resonant Path Approximation

It is interesting to investigate the form of the resonant paths in the vicinity of the boundaries. A general resonant field line will satisfy the condition $\omega_A(x, y, \theta_r) = \omega_d$. Now consider the subset of field lines that sit on a particular resonant path. The path is defined by the value of the F on the contour $F(x, y, \omega_d) = const$. We can now use s as a parameter along this path, and also for the corresponding value of θ_r on it. Hence, the resonant condition for this particular path becomes $\omega_A(x(s), y(s), \theta_r(s)) = \omega_d$. Taking d/ds of this equation and rearranging for $d\theta_r/ds$ gives

$$\frac{d\theta_r}{ds} = -\left(\frac{\partial\omega_A}{\partial x}\frac{dx}{ds} + \frac{\partial\omega_A}{\partial y}\frac{dy}{ds}\right)\Big/\frac{\partial\omega_A}{\partial\theta}. \tag{11}$$

This shows that θ_r changes very rapidly with path length s near the boundary as $\partial\omega_A/\partial\theta$ will be very small. (Indeed it goes to zero on the boundary.)

This can also be appreciated by considering the $\omega_A(\theta)$ curves like those depicted in Figure 1c: on the boundary $\theta_r = \theta_{max}$ (curve 1). On moving a small increment ds along the path the $\omega_A(\theta)$ curve will shift slightly, perhaps taking a step toward adopting form of curve 2. The parabolic nature of the curve can relate the change in ω_{Amax}, $\delta\omega_{Amax}$, and the change in θ_r, $\delta\theta_r$, for this step approximately by $\delta\omega_{Amax} \sim \delta\theta_r^2$. Hence a small increment $\delta\theta_r$ corresponds to an even smaller increment $\delta\omega_{Amax}$. This is equivalent to saying that a small change in $\delta\omega_{Amax}$ on stepping along the path will have a corresponding much larger change in θ_r, so the path turns relatively quickly.

To explore the form of the Resonant Paths in the vicinity of a Resonant Zone boundary, we consider the boundary given by $\Gamma_m(x, y) = 0$. (Here the boundary is the set of points $(x, y) = (x_m, y_m)$, and m can be either max or min.) The leading terms in a Taylor series expansion of $\omega_A(x, y, \theta)$ about the values of x, y, and θ on the boundary (i.e., x_m, y_m, and θ_m) has the form

$$\omega_A(x, y, \theta) = \omega_A(x_m, y_m, \theta_m) + a_x(x - x_m) + a_y(y - y_m) + b(\theta - \theta_m(x_m, y_m))^2 \tag{12}$$

with coefficients

$$a_x = \left.\frac{\partial\omega_A}{\partial x}\right|_{y,\theta}, \qquad a_y = \left.\frac{\partial\omega_A}{\partial y}\right|_{x,\theta}, \qquad b = \frac{1}{2}\left.\frac{\partial^2\omega_A}{\partial\theta^2}\right|_{x,y}. \tag{13}$$

Once the partial derivatives have been taken, they are evaluated at the expansion point (x_m, y_m, θ_m) for use in Equation 12.

Recall that on a Resonant Path $\omega_A(x, y, \theta) = \omega_d$, and where this path intersects the Resonant Zone boundary (i.e., $x = x_m$, $y = y_m$) the resonant polarization angle is θ_m. Evaluating the series expansion (Equation 12) at this point gives the leading term to be $\omega_A(x_m, y_m, \theta_m) = \omega_d$.

As the path moves inside the Resonant Zone (but remains near the boundary) the resonant condition ($\omega_A(x, y, \theta_r) = \omega_d$) can be used with Equation 12 to evaluate $\theta_r(x, y)$ as

$$\theta_r(x, y) = \theta_m(x_m, y_m) \pm \sqrt{-\frac{a_x(x - x_m) + a_y(y - y_m)}{b}}. \tag{14}$$

Substitution of Equation 14 into Equation 8 gives the differential equation for the Resonant Path that is valid in the vicinity of the boundary,

$$\frac{dx}{dy} = \tan\left(\theta_m(x_m, y_m) \pm \sqrt{-\frac{a_x(x - x_m) + a_y(y - y_m)}{b}}.\right) \tag{15}$$

To illustrate the use of this approximation further we consider a Resonance Map like that in Figure 2a where the boundaries correspond to the poloidal and toroidal polarizations and are independent of y. We also compare the approximate paths with the exact solution determined using a numerical solution.

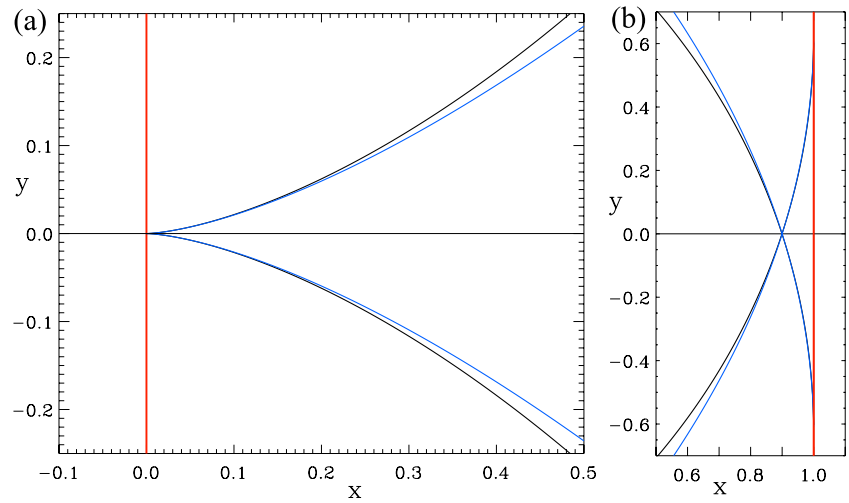

Figure 3. Resonant paths near the Resonant Zone boundaries. The exact solution is plotted in black, and the approximation in blue. The Resonant Zone boundaries are shown in red. The Resonant Paths are qualitatively similar to those in Figure 2a: (a) Resonant paths near the poloidal boundary for $x_{min} = 0$, $a_x = -1$, and $b = 1$. (b) Resonant paths near the toroidal boundary for $x_{max} = 1$, $a_x = -1$, and $b = -1$.

3.1. Poloidal Boundary Example

Let the poloidal boundary be located at $x = x_{min}$. In Equation 12 we let m represent min and set $\theta_{min} = \pi/2$ and note $a_y = 0$ to get

$$\omega_A(x, y, \theta) = \omega_d + a_x(x - x_{min}) + b(\theta - \pi/2)^2. \tag{16}$$

As this is for the poloidal boundary ($\omega_{Amin}(x_{min}, \theta_{min}) = \omega_d$) we require $b(x_{min}) > 0$. If $a_x < 0$ the Resonant Zone will lie in the region $x > x_{min}$.

The two resonant polarization angles are,

$$\theta_r^+ = \pi/2 + \sqrt{-\frac{a_x(x - x_{min})}{b}}, \qquad \theta_r^- = \pi/2 - \sqrt{-\frac{a_x(x - x_{min})}{b}}, \tag{17}$$

and the differential equations of the two paths are

$$\frac{dy^+}{dx} = \cot\left(\theta_r^+\right) = -\tan\left(\sqrt{-\frac{a_x(x - x_{min})}{b}}\right), \qquad \frac{dy^-}{dx} = \cot(\theta_r^-) = +\tan\left(\sqrt{-\frac{a_x(x - x_{min})}{b}}\right). \tag{18}$$

When near the boundary the arguments of the tangent functions are small, and to leading order $\tan(\delta) \approx \delta$, ($\delta \ll 1$). These assumptions give the approximate analytical solutions

$$y^+ \approx y_{min} - \frac{2}{3}\sqrt{-\frac{a_x(x - x_{min})^3}{b}}, \qquad y^- \approx y_{min} + \frac{2}{3}\sqrt{-\frac{a_x(x - x_{min})^3}{b}} \tag{19}$$

Figure 3a shows the approximate and exact solutions for the two paths at the poloidal boundary. The agreement may be improved further by taking more terms in the expansion (Equation 16) and the tangent power series, although this will eventually lead to equations that to not have an analytical solution.

3.2. Toroidal Boundary Example

Let the toroidal boundary be located at $x = x_{max}$. In Equation 12 we let m represent max and set $\theta_{max} = 0$ and note $a_y = 0$ to get

$$\omega_A(x, y, \theta) = \omega_d + a_x(x - x_{max}) + b\theta^2. \tag{20}$$

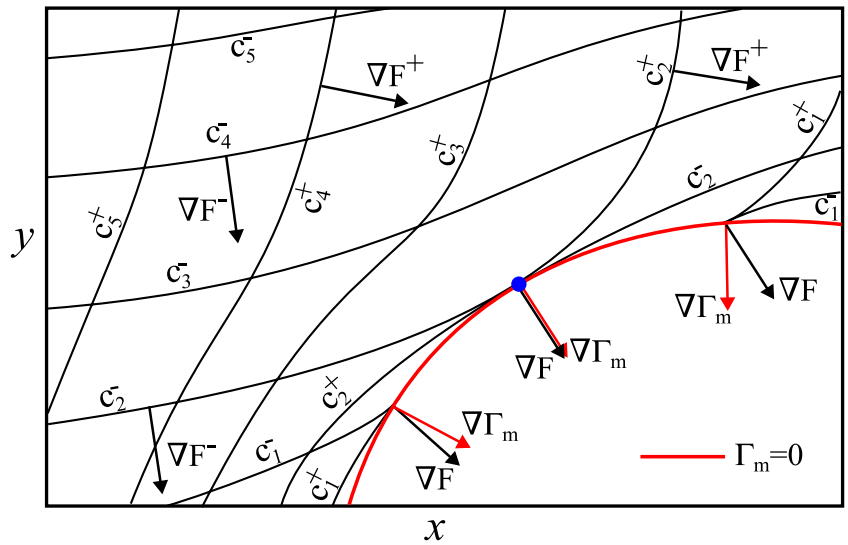

Figure 4. A close up view of the Resonant Zone boundary (red) and Resonant Paths (black). Resonant paths are given by contours of $F^{\pm}$, for example, $F^{\pm} = c_3^{\pm}$, where the c's are constants. The directions of ∇F and $\nabla\Gamma_m$ are indicated by the black and red arrows, respectively.

As ω_A is a maximum at this boundary we require $b < 0$. For consistency with Figure 2a and Section 3.1 we need $x_{max} > x_{min}$ and the Resonant Zone lies to the left of x_{max}, which requires $a_x < 0$. Rearranging Equation 20 the resonant polarization angles are

$$\theta_r^+ = +\sqrt{-\frac{a_x(x - x_{max})}{b}}, \qquad \theta_r^- = -\sqrt{-\frac{a_x(x - x_{max})}{b}}. \tag{21}$$

As $dy/dx \to \infty$ as $x \to x_{max}$ it is easier to work with the equation for dx/dy.

$$\frac{dx^+}{dy} = \tan\left(\theta_r^+\right) = \tan\left(\sqrt{-\frac{a_x(x^+ - x_{max})}{b}}\right), \qquad \frac{dx^-}{dy} = -\tan(\theta_r^-) = -\tan\left(\sqrt{-\frac{a_x(x^- - x_{max})}{b}}\right). \tag{22}$$

Again, near the boundary we can use the leading term in the tangent series to get the analytical approximations

$$y^+ \approx y_{max} - 2\sqrt{-\frac{b(x - x_{max})}{a_x}}, \qquad y^- \approx y_{max} + 2\sqrt{-\frac{b(x - x_{max})}{a_x}}. \tag{23}$$

Figure 3b shows good agreement near the toroidal boundary between the approximation in Equation 23 and the exact numerical solution.

4. Efficient Coupling as a Minimization Principle

It has been demonstrated that there are an infinite number of Resonant Paths within the Resonant Zone (Elsden et al., 2022; Wright & Elsden, 2016). Normally one or two of these paths are needed to identify the location of the resonant Alfvén waves excited by the fast mode in a particular simulation. Wright et al. (2022) showed how the "tangential alignment condition" could be used to identify locations where efficient Alfvén wave excitation takes place, and hence the relevant paths emerging from these points on which the largest Alfvén waves are excited. This is illustrated in Figure 4, which could describe either the $\Gamma_{max} = 0$ or $\Gamma_{min} = 0$ boundary, so we denote it, again, by $\Gamma_m = 0$ and the red line. Note that as $\Gamma_m(x, y, \omega_d)$ is constant along this line, $\nabla\Gamma_m$ will be perpendicular to it, as indicated by the red arrows.

In Section 2.2 it was shown that the Resonant Paths correspond to contours of the function $F(x, y, \omega_d)$. Moreover, at any point inside the Resonant Zone there will be two possible paths corresponding to the two values of θ_r.

Figure 4 distinguishes between these two families of paths through the functions F^+ and F^-. The black lines show Resonant Paths corresponding to the contours $F^+ = c_1^+, c_2^+, \ldots, c_5^+$, and $F^- = c_1^-, c_2^-, \ldots, c_5^-$. For points (x, y) inside the Resonant Zone there are two paths through it given by $F^+ = c^+$ and $F^- = c^-$. Evidently, ∇F^+ and ∇F^- are perpendicular to their contours, and the direction is shown by the black arrows.

As the Resonant Paths approach the boundary the two single root polarization angles θ_r^+ and θ_r^- converge to a single double root. Hence, the directions ∇F^+ and ∇F^- become the same on the boundary, so we denote it by ∇F there and indicate its direction by black arrows. In Figure 4 we can see that the contours with values c_1^+ and c_1^- intersect the boundary at a nonzero angle given by the angle between the red and black arrows. The situation is different for the c_2^+ and c_2^- contours which meet the boundary at the blue dot where ∇F and $\nabla \Gamma_m$ are aligned as shown by the red and black arrows.

The alignment of ∇F and $\nabla \Gamma_m$ is equivalent to stating that the Resonant Paths are tangential to the Resonant Zone boundary. Indeed this is the "tangential alignment condition" proposed by Wright et al. (2022) for identifying where efficient resonant excitation occurs. The fact that this is equivalent to requiring ∇F and $\nabla \Gamma_m$ to align on the boundary is significant, as this can now be recognised as a Lagrange Multiplier minimization problem.

Consider the Lagrangian function, G, defined as

$$G(x, y, \omega_d, \lambda) = F(x, y, \omega_d) - \lambda \Gamma_m(x, y, \omega_d), \tag{24}$$

where λ is a Lagrange Multiplier. F can be either F^+ or F^- in Equation 24. Taking partial derivatives w.r.t x, y, and λ and equating to zero gives the stationary points of G.

$$\frac{\partial F}{\partial x} = \lambda \frac{\partial \Gamma_m}{\partial x} \tag{25}$$

$$\frac{\partial F}{\partial y} = \lambda \frac{\partial \Gamma_m}{\partial y} \tag{26}$$

$$\Gamma_m = 0. \tag{27}$$

These are three equations for the unknowns x, y, and λ. Equation 27 means we are only considering points on the Resonant Zone boundary $\Gamma_m = 0$. Equations 25 and 26 are equivalent to the components of

$$\nabla F(x, y, \omega_d) = \lambda \nabla \Gamma_m(x, y, \omega_d) \tag{28}$$

so the direction of ∇F and $\nabla \Gamma_m$ are parallel or anti-parallel. As already mentioned, Resonant Paths are contours of F, so ∇F is oriented perpendicular to these paths. The Resonant Zone boundary is the zero contour of Γ_m, so $\nabla \Gamma_m$ is normal to it on the boundary. Hence, Equations 25–27 are identifying the points on the Resonant Zone boundary ($\Gamma_m = 0$) where the normal to the boundary ($\nabla \Gamma_m$) and the normal to the Resonant Paths (∇F) are aligned. This will correspond to the point on the boundary where the Resonant Path is tangential to the Resonant Zone boundary, that is, the tangential alignment condition is satisfied.

In terms of the Lagrange multiplier formulation, the tangential alignment condition corresponds to finding the minimum (or maximum) value of F on the boundary. This is interesting as such minimization constraints often point to some deeper truth of the nature of the system considered. To help explore this matter further we give a worked analytical example in the next section.

4.1. Minimization of F Example

In this section we assume the equilibrium magnetic field is a 2D line dipole aligned with y, as used in Wright and Elsden (2016). If the density is also independent of y the equilibrium would be entirely 2D, and a monotonic variation of ω_A with x would produce a Resonance Map like that in Figure 2a. In this example we make the equilibrium 3D by allowing the density to vary periodically with y such that the $\omega_{Amax} = \omega_d$ boundary is given by $\Gamma_{max} = 0$, where

$$\Gamma_{max} = x - y_0 \sin(ky). \tag{29}$$

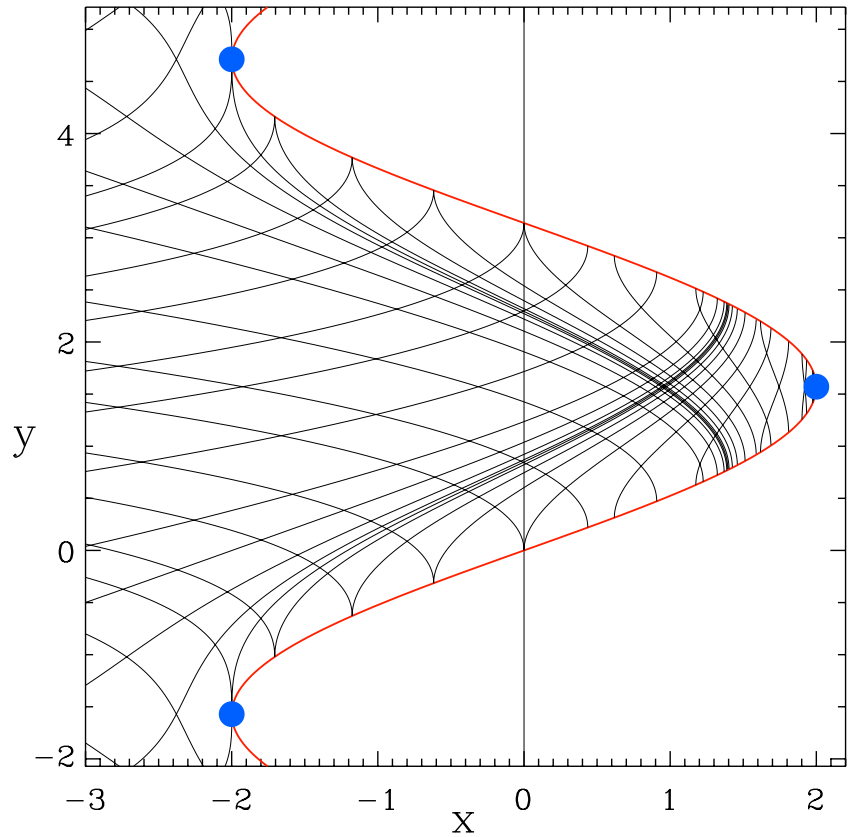

Figure 5. A plot of the Resonant Zone boundary (red) and Resonant Paths (black) for $y_0 = 2$, $k = 1$, and $L = 1$. The blue dots indicate where the tangential alignment condition is satisfied. These locations are also where maxima or minima of $F^{\pm}$ occur on the boundary.

Here k is a constant determining the periodicity in y, and y_0 controls the degree of deviation from the 2D case. Figure 5 shows the Resonant Zone boundary as the red line corresponding to the points $(x, y) = (x_{\max}, y_{\max})$ where $x_{\max}(y_{\max}) = y_0 \sin(k y_{\max})$.

To keep the analysis analytical we assume the density variation in x and z is tailored to give

$$\tan(\theta_r(x, y, \omega_d)) = f_2(x, y, \omega_d) = \pm(x - y_0 \sin(ky))/L. \tag{30}$$

This choice gives $\theta_r = 0$ on $\Gamma_{\max} = 0$, so corresponds to the toroidal boundary. The Resonant Zone lies to the left of this boundary. L is the length scale that $\tan(\theta_r)$ changes with in x.

The equations for the two resonant paths are (see Equation 8)

$$\frac{dx^+}{dy} = \frac{x - y_0 \sin(ky)}{L} \tag{31}$$

$$\frac{dx^-}{dy} = -\frac{x - y_0 \sin(ky)}{L} \tag{32}$$

Integration gives a relation between x and y and an integration function $F^{\pm}$ that is constant on a characteristic. Rearranging for F gives.

$$F^+(x^+, y) = \frac{\left(1 + k^2L^2\right)x^+ - (kL\cos(ky) + \sin(ky))y_0}{1 + k^2L^2}\exp(-y/L) \tag{33}$$

$$F^-(x^-, y) = \frac{\left(1 + k^2L^2\right)x^- + (kL\cos(ky) - \sin(ky))y_0}{1 + k^2L^2}\exp(y/L) \tag{34}$$

It is straightforward to show that differentiating Equations 33 and 34, to find $\partial F^{\pm}/\partial x^{\pm}$ and $\partial F^{\pm}/\partial y$, together with the first half of Equation 10 recovers Equations 31 and 32.

The value of $F^{\pm}$ on the boundary can be found by substituting $x^{\pm} = x_{\max}(y_{\max}) = y_0 \sin(ky_{\max})$ and $y = y_{\max}$ to give $F^{\pm}(x_{\max}(y_{\max}), y_{\max})$. Hence the value of $F^{\pm}$ on the boundary is parameterized in terms of $y_{\max}$, and we denote this by $F^{\pm}_{\mathrm{B}}(y_{\max})$. Substitution in Equations 33 and 34 gives.

$$F^{+}_{\mathrm{B}}(y_{\max}) = (kL\ \sin(ky_{\max}) - \cos(ky_{\max}))\frac{y_0 kL}{k^2L^2+1}\exp(-y_{\max}/L) \tag{35}$$

$$F^{-}_{\mathrm{B}}(y_{\max}) = (kL\ \sin(ky_{\max}) + \cos(ky_{\max}))\frac{y_0 kL}{k^2L^2+1}\exp(y_{\max}/L). \tag{36}$$

The form of the paths leaving the boundary at $(x, y) = (x_{\max}(y_{\max}), y_{\max})$ can be traced into the resonant zone by recalling that F is constant along these paths. Hence equating $F^{+}(x^{+}, y) = F^{+}_{\mathrm{B}}(y_{\max})$ and $F^{-}(x^{-}, y) = F^{-}_{\mathrm{B}}(y_{\max})$ will give two equations for $x^{+}(y)$ and $x^{-}(y)$ that originate from the boundary point $(x_{\max}(y_{\max}), y_{\max})$. The explicit forms are

$$x^{+}(y) = \frac{y_0}{k^2L^2+1}\left(\sin(ky) + kL\ \cos(ky) + kL[kL\ \sin(ky_{\max}) - \cos(ky_{\max})]\exp\left(\frac{y-y_{\max}}{L}\right)\right) \tag{37}$$

$$x^{-}(y) = \frac{y_0}{k^2L^2+1}\left(\sin(ky) - kL\ \cos(ky) + kL[kL\ \sin(ky_{\max}) + \cos(ky_{\max})]\exp\left(\frac{y_{\max}-y}{L}\right)\right) \tag{38}$$

and they are plotted as the black lines in Figure 5. Evidently, the Resonant Paths are tangential to the Resonant Zone boundary at $y = \left(n+\frac{1}{2}\right)\pi$, and are highlighted with the blue dots in the figure. We can check the claim that $F^{\pm}$ max/minimizes on the boundary at these points by differentiating Equations 35 and 36 to find where $F^{\pm}_{B}$ have their maxima and minima.

$$\frac{dF^{+}_{\mathrm{B}}}{dy_{\max}} = y_0 k\ \cos(ky_{\max})\exp(-y_{\max}/L),\ \ = 0 \Rightarrow ky_{\max} = \left(n+\frac{1}{2}\right)\pi, \tag{39}$$

$$\frac{dF^{-}_{\mathrm{B}}}{dy_{\max}} = y_0 k\ \cos(ky_{\max})\exp(+y_{\max}/L),\ \ = 0 \Rightarrow ky_{\max} = \left(n+\frac{1}{2}\right)\pi. \tag{40}$$

Recalling that Figure 5 was constructed by adopting $k = 1$, we see the blue dots do indeed correspond to the locations where $F^{\pm}_{B}$ have their extrema.

5. Concluding Remarks

Use of the tangential alignment condition to identify locations of strong wave coupling has been demonstrated in numerical simulations reported by Wright et al. (2022). The tangential alignment condition means that strongly excited resonant Alfvén waves exist on Resonant Paths that meet the Resonant Zone boundary tangentially. As the plasma displacement is along these paths, it means the Alfvén wave plasma displacement (as well as velocity and magnetic field perturbations) will also be tangential to the Resonant Zone boundary. So long as there is some component of the fast mode magnetic pressure gradient along this Resonant Path, we can expect a large amplitude resonant Alfvén wave to be excited on it.

The situation is different on paths that do not satisfy the tangential alignment condition. Consider the Resonant Paths emerging from the Resonant Zone boundary at $(x, y) = (0,0)$ in Figure 5 that approach the boundary at an angle of about 60°. If field lines on these paths just inside the Resonant Zone have a large amplitude resonant Alfvén wave established on them, it raises the question of how $\nabla \cdot \mathbf{b} = 0$ is maintained: the normal component of $\mathbf{b}$ across the Resonant Zone boundary must be continuous and suggests that there must be a correspondingly large Alfvén wave just outside the Resonant Zone. This is unlikely as the field lines here are responding non-resonantly, so will be of smaller amplitude. This is not a problem for the tangential alignment point at $y = -2$ in Figure 5 as the corresponding paths remain in the Resonant Zone.

It is interesting to consider what happens when a Resonant Path satisfies the tangential alignment condition at one point (e.g., $(x, y) = (-2, 4.7)$, so has a large amplitude resonant Alfvén wave excited on it), but the path goes on to

meet the zone boundary elsewhere ($(x, y) = (1.4, 0.7)$) where it is not tangential. Wright and Elsden (2016) show how the system resolves the issue by having resonant Alfvén waves present on both paths at (1.4, 0.7), that is, the one traced to left and the one traced to the right. Presumably, the normal Alfvén wave magnetic field from one path largely cancels that from the other at the boundary. Any remaining normal magnetic field could be balanced outside of the Resonant Zone by a non-resonant Alfvén wave. Figure 7 of Wright and Elsden (2016) clearly shows how the combination of Alfvén waves on two such paths reduces the total Alfvén wave energy, and hence wave fields, where the two overlap as they approach the boundary. The paths from tangential alignment point in Figure 5 at $x = 2$ find themselves in the situation of encountering the boundary immediately. Numerical solutions show that the resonant Alfvén waves lie on paths forming a criss-cross pattern bouncing between successive encounters with the boundary (Wright & Elsden, 2016; Wright et al., 2022). The behavior of the wave fields at such a boundary intersection warrants further theoretical development.

A complete analytical theory of resonant Alfvén wave excitation in 3D equilibria is still to be developed. The existence of the Resonant Zone (which is absent in 1D and 2D equilibria) and the multiplicity of permissible Resonant Paths are the main new features that need to be incorporated. The recent advances in this area have come from simulations that reveal the key properties any analytical theory will need to accommodate. The tangential-alignment condition is one such property. In this paper, we have shown that it is equivalent to a minimization principle. Such principles can provide an alternative formulation which may be useful for making future progress or consolidating our current understanding.

A remaining open question is what the significance of the efficient resonant wave coupling criterion being derivable from a minimization principle is. A useful step to answering this may be to consider what the quantity F_B could correspond to physically. Of course, if F_B is minimized, then a function of F_B is also likely to be minimized (or maximized). Further worked examples like the one in Section 4 may facilitate progress and reveal a physical meaning of the minimization problem, which could be of value.

Data Availability Statement

No data was used in this research.

Acknowledgments
The author was partially funded by STFC Grant ST/W001195/1. The support of the International Space Science Institute (ISSI) in Bern is gratefully acknowledged. The writing of this article was completed as part of the activities of ISSI International Team project 483 (The Identification And Classification Of 3D Alfvén Resonances).

References

Allan, W., Poulter, E. M., & White, S. P. (1986). Hydromagnetic wave coupling in the magnetosphere–plasmapause effects on impulse-excited resonances. *Planetary and Space Science*, *34*(12), 1189–1200. https://doi.org/10.1016/0032-0633(86)90056-5

Chen, L., & Hasegawa, A. (1974). A theory of long-period magnetic pulsations: 1. Steady state excitation of field line resonance. *Journal of Geophysical Research*, *79*(7), 1024–1032. https://doi.org/10.1029/JA079i007p01024

Cheng, C. Z. (2003). MHD field line resonances and global modes in three-dimensional magnetic fields. *Journal of Geophysical Research*, *108*(A1), 1002. https://doi.org/10.1029/2002JA009470

Degeling, A. W., Rae, I. J., Watt, C. E. J., Shi, Q. Q., Rankin, R., & Zong, Q. G. (2018). Control of ULF wave accessibility to the inner magnetosphere by the convection of plasma density. *Journal of Geophysical Research: Space Physics*, *123*(2), 1086–1099. https://doi.org/10.1002/2017JA024874

Degeling, A. W., Rankin, R., Kabin, K., Rae, I. J., & Fenrich, F. R. (2010). Modeling ULF waves in a compressed dipole magnetic field. *Journal of Geophysical Research*, *115*(A10), A10212. https://doi.org/10.1029/2010JA015410

Dungey, J. W. (1954). *Electrodynamics of the outer atmosphere: Report to National Science Foundation on work carried on under grant NSF-G450*. Pennsylvania State University, Ionosphere Research Laboratory. Retrieved from https://books.google.co.uk/books?id=3NrUAAAAMAAJ

Elsden, T. (2016). *Numerical modelling of ultra low frequency waves in Earth's magnetosphere* (Doctoral dissertation). University of St Andrews. Retrieved from http://hdl.handle.net/10023/15663

Elsden, T., Wright, A., & Degeling, A. (2022). A review of the theory of 3-D Alfvén (field line) resonances. *Frontiers in Astronomy and Space Sciences*, *9*, 917817. https://doi.org/10.3389/fspas.2022.917817

Feynman, R. P. (1964). Feynman lectures on physics. Volume 2. Mainly electromagnetism and matter.

Goedbloed, J. P. (1975). Spectrum of ideal magnetohydrodynamics of axisymmetric toroidal systems. *Physics of Fluids*, *18*(10), 1258–1268. https://doi.org/10.1063/1.861012

Goossens, M., Erdélyi, R., & Ruderman, M. S. (2011). Resonant MHD waves in the solar atmosphere. *Space Science Reviews*, *158*(2–4), 289–338. https://doi.org/10.1007/s11214-010-9702-7

Goossens, M., Ruderman, M. S., & Hollweg, J. V. (1995). Dissipative MHD solutions for resonant Alfvén waves in 1-dimensional magnetic flux tubes. *Solar Physics*, *157*(1–2), 75–102. https://doi.org/10.1007/BF00680610

Mann, I. R., Wright, A. N., & Cally, P. S. (1995). Coupling of magnetospheric cavity modes to field line resonances: A study of resonance widths. *Journal of Geophysical Research*, *100*(A10), 19441–19456. https://doi.org/10.1029/95JA00820

Pao, Y.-P. (1975). The continuous MHD spectrum in toroidal geometries. *Nuclear Fusion*, *15*(4), 631–635. https://doi.org/10.1088/0029-5515/15/4/008

Poedts, S., Goossens, M., & Kerner, W. (1989). Numerical simulation of coronal heating by resonant absorption of Alfvén waves. *Solar Physics*, *123*(1), 83–115. https://doi.org/10.1007/BF00150014

Samson, J. C., Jacobs, J. A., & Rostoker, G. (1971). Latitude-dependent characteristics of long-period geomagnetic micropulsations. *Journal of Geophysical Research*, *76*(16), 3675–3683. https://doi.org/10.1029/JA076i016p03675

Singer, H. J., Southwood, D. J., Walker, R. J., & Kivelson, M. G. (1981). Alfven wave resonances in a realistic magnetospheric magnetic field geometry. *Journal of Geophysical Research*, *86*(A6), 4589–4596. https://doi.org/10.1029/JA086iA06p04589

Southwood, D. J. (1974). Some features of field line resonances in the magnetosphere. *Planetary and Space Science*, *22*(3), 483–491. https://doi.org/10.1016/0032-0633(74)90078-6

Terradas, J., Soler, R., Luna, M., Oliver, R., Ballester, J. L., & Wright, A. N. (2016). Solar prominences embedded in flux ropes: Morphological features and dynamics from 3D MHD simulations. *Astrophysical Journal*, *820*(2), 125. https://doi.org/10.3847/0004-637X/820/2/125

Thompson, M. J., & Wright, A. N. (1993). Resonant Alfven wave excitation in two-dimensional systems – Singularities in partial differential equations. *Journal of Geophysical Research*, *98*(A9), 15–15551. https://doi.org/10.1029/93JA00791

Tirry, W. J., & Goossens, M. (1995). Dissipative MHD solutions for resonant Alfvén waves in two-dimensional poloidal magnetoplasmas. *Journal of Geophysical Research*, *100*(A12), 23687–23694. https://doi.org/10.1029/95JA02691

Van Doorsselaere, T., Srivastava, A. K., Antolin, P., Magyar, N., Vasheghani Farahani, S., Tian, H., et al. (2020). Coronal heating by MHD waves. *Space Science Reviews*, *216*(8), 140. https://doi.org/10.1007/s11214-020-00770-y

Wright, A. N., Degeling, A. W., & Elsden, T. (2022). Resonance Maps for 3D Alfvén waves in a compressed dipole field. *Journal of Geophysical Research: Space Physics*, *127*(4), e30294. https://doi.org/10.1029/2022JA030294

Wright, A. N., & Elsden, T. (2016). The theoretical foundation of 3D Alfvén resonances: Normal modes. *Astrophysical Journal*, *833*(2), 230. https://doi.org/10.3847/1538-4357/833/2/230

Wright, A. N., & Elsden, T. (2023). Resonant fast-Alfvén wave coupling in a 3D coronal arcade. *Physics*, *5*(1), 310–321. https://doi.org/10.3390/physics5010023

Wright, A. N., & Thompson, M. J. (1994). Analytical treatment of Alfvén resonances and singularities in nonuniform magnetoplasmas. *Physics of Plasmas*, *1*(3), 691–705. https://doi.org/10.1063/1.870815